Cryo-EM structure of the bicarbonate receptor GPR30

Shota Kaneda[1], Airi Jo-Watanabe[2‡], Hiroaki Akasaka[1], Hidetaka S. Oshima[1], Takehiko Yokomizo[2], Wataru Shihoya[1‡], Osamu Nureki[1‡].

Affiliations:

[1]Department of Biological Sciences, Graduate School of Science, The University of Tokyo, Bunkyo, Tokyo 113-0033, Japan.

[2]Department of Biochemistry, Juntendo University Graduate School of Medicine, Tokyo 113-8421, Japan.

‡ To whom correspondence should be addressed. E-mail: awatanabe-tky@umin.ac.jp (A.J.-W), wtrshh9@gmail.com (W.S.), and nureki@bs.s.u-tokyo.ac.jp (O.N.)

ORCID list
Airi Jo-Watanabe 0000-0002-5219-1553
Hiroaki Akasaka 0000-0003-2118-0912
Hidetaka S. Oshima 0009-0000-0341-707X
Takehiko Yokomizo 0000-0003-0899-9915
Wataru Shihoya 0000-0003-4813-5740
Osamu Nureki 0000-0003-1813-7008

Abstract

G-protein-coupled receptor 30 (GPR30) is a bicarbonate receptor that plays a vital role in cellular responses to extracellular pH and ion homeostasis. Despite its significance, the mechanisms by which GPR30 interacts with bicarbonate ions remain elusive. There is no consensus on a drug that targets GPR30, and the difficulty in the pharmacological analysis has limited biological and drug discovery researches on GPR30. Here, we present the cryo-electron microscopy structure of human GPR30 in the presence of bicarbonate ions at 3.2 Å resolution. Our structure reveals unique extracellular pockets and critical residues for bicarbonate binding and activation. Functional assays demonstrate that mutations in these residues impair bicarbonate-induced GPR30 activation, underscoring their importance in receptor function. This study also provides insights into the G-protein coupling, highlighting the structural divergence between GPR30 and other GPCRs. Our findings not only advance the understanding of the role of GPR30 in pH homeostasis but also pave the way for the development of high-affinity drugs targeting GPR30 for therapeutic interventions in diseases associated with acid-base imbalance.

Introduction

The extracellular environment regulates cellular responses, as exemplified by pH and ion homeostasis. The acid-base balance, largely based on the bicarbonate buffer system *in vivo*, serves as a vital mechanism that maintains the optimal pH for cellular function.[1] Changes in the extracellular pH and ion homeostasis are monitored by membrane channels and receptors, such as G protein-coupled receptors (GPCRs). However, it remains unknown whether and how the acid–base balance-related ions, protons and bicarbonate ions, bind to the receptors and cause conformational changes that lead to intracellular signal transduction.

Previous studies established four acid–base balance-related GPCRs[2–4] that respond to an increase in proton concentration. None of the structures of these proton-sensing GPCRs in a proton-bound form has been determined, although the cryo-EM

structures of apo-GPR134 (G2A) and its oxidized fatty acid- and N-acyl amino acid-bound forms have been reported.[5] While these proton-sensing GPCRs are likely to be involved in pH homeostasis, particularly in the acidic tumor microenvironment, at inflamed sites, and in ischemia-reperfusion injury[6], it remains unknown how protons cooperate with these receptors working as acid–base balance-related GPCRs.

We recently reported that the physiological concentration of bicarbonate ions, a counterpart of protons in the bicarbonate buffer system, activates G protein-coupled receptor 30 (GPR30), which leads to G_q-coupled calcium responses[7]. Our study also demonstrated that GPR30 in brain mural cells regulates blood flow and ischemia–reperfusion injury. GPR30 was identified as a G protein-coupled estrogen receptor that mediates the rapid non-genomic action of estradiol (E2)[8]. However, despite numerous reports on the pleiotropic functions of GPR30 *in vivo*[9,10], there is controversy surrounding the responses of GPR30 to E2 *in vitro*[11], *ex vivo*[12], and *in vivo*[13]. The broad expression of Gpr30[14,15], including blood vessels[16,17], stomach, and lung, has also raised the possibility of its non-estrogenic functions. We demonstrated that three amino acids, E115, Q138, and H307, are essential for the bicarbonate-induced activation of GPR30, according to the public homology model (https://gpcrdb.org/)[18]. However, we did not examine whether bicarbonate ions interact with GPR30 and cause conformational changes. Moreover, to date, there is no consensus on a high-affinity drug that targets GPR30, and the difficulty in the pharmacological analysis has limited biological and drug discovery research on GPR30. To elucidate the bicarbonate–GPR30 interaction and to clarify the first structural identification of an acid-base balance-related GPCR, we report the cryo-electron microscopy (cryo-EM) structure of human GPR30 in the presence of bicarbonate ions.

Results

Overall structure

For the structural study, we used the full-length human GPR30 sequence. To efficiently purify the stable GPCR-G-protein complex, the receptor and mini-G_{sqi} were incorporated in a 'Fusion-G system' by combining two complex stabilization techniques[19,20] (Figure 1—figure supplement 1A, B). The modified receptor and G-

79 protein were co-expressed in HEK293 cells and purified by Flag affinity chromatography
80 in the presence of 200 mM $NaHCO_3$. After an incubation with nanobody 35 (Nb35) and
81 single chain scFv16, which binds to mini-G_{sqi}, the complex was purified by size exclusion
82 chromatography (Figure 1—figure supplement 1C, D). The structure of the purified
83 complex was determined by single-particle cryo-EM analysis, with an overall resolution
84 of 3.21 Å (Table 1, Figure 1—figure supplement 2, and "Methods"). As the extracellular
85 portion of the receptor was poorly resolved, we performed receptor focused refinement,
86 yielding a density map with a nominal resolution of 3.30 Å, which was combined with
87 the overall refined map. The resulting composite map allowed us to precisely build the
88 atomic model of the components, including the receptor (residues 51 to 196, 207 to 288,
89 and 296 to 340, G-proteins, and scFv16 (Figure 1A, B). Nb35 was not visible in the cryo-
90 EM map, probably because of the effect of the mini-G_s modification, although the
91 interactive residues with Nb35 were not changed.
92 The receptor consists of the canonical 7 transmembrane helices (TM) connected by
93 three intracellular loops (ICL1–3) and three extracellular loops (ECL1–3), and the
94 amphipathic helix 8 at the C-terminus (H8) (Figure 2A). Most of the TMs are kinked as
95 in typical GPCRs[21], but TM1 is also kinked at $P71^{1.44}$ (superscripts indicate Ballesteros-
96 Weinstein numbers[22]), whereas TM1 adopts a straight α-helix in most class A GPCRs.
97 ICL1 and ECL1 contain short α helices (Figure 2B, C). The short ICL3 was completely
98 visible in the cryo-EM map (Figure 2C and Figure 1—figure supplement 3), while
99 residues 197 to 206 in ECL2 and 289 to 295 in ECL3 were disordered (Figure 2B). ECL2
100 is attached to ECL1 by the disulfide bond between $C130^{ECL1}$ and $C207^{ECL2}$ (Figure 2B),
101 which is highly conserved in class A GPCRs[21]. The cryo-EM structure did not
102 superimpose well on the AlphaFold-predicted structure (Q99527 in the AlphaFold
103 [19,20]database) with a root mean square deviation (R.M.S.D.) of Cα atoms of 2.33 Å (Figure
104 2—figure supplement 1A). The conserved $D^{3.49}R^{3.50}Y^{3.51}$ motif[21] in the predicted
105 structure represents an inactive state (Figure 2—figure supplement 1B). Moreover, ECLs
106 2 and 3 are rich in cysteine residues, which form incorrect disulfide bonds in the predicted
107 structure (Figure 2—figure supplement 1C). These comparisons support the usefulness
108 of experimental structural determination.
109

110 **Extracellular pockets**

111 The interaction network between ECL1–3 covers the extracellular side of the
112 receptor: ECL2 is anchored to ECL1 via the disulfide bond and ECL3 extends between
113 ECL1 and ECL2, with Q296$^{7.25}$ and F298$^{7.27}$ located within the receptor cavity (Figure
114 3A). R299^{ECL3} and the backbone carbonyl oxygen of S297^{ECL3} interact with D210^{ECL2},
115 and N296$^{7.25}$ forms polar interactions with E115$^{2.60}$, Q121$^{2.66}$, and N310$^{7.39}$. These
116 interactions among the ECLs create four extracellular pockets (Pockets A–D) (Figure
117 3B). While Pockets A–C are positively-charged , Pocket D is negatively, and the size of
118 each pocket is varied. Pocket A consists of ECL1, TM1, and TM7 (Figure 3C), while
119 pocket B is formed by TM6, TM7, and ECL1 (Figure 3D). These two pockets are
120 separated by R122^{ECL1} and H307$^{7.36}$. Pocket A is hydrophobic and appears unsuitable for
121 bicarbonate binding (Figure 3C). Pocket B has hydrophilic residues (Figure 3D), but
122 given the invisible region of ECL3 (residues 289 to 295), we cannot rule out the
123 possibility that the pocket is buried. Pocket C consists of ECL2, ECL3, TM5, and TM6,
124 and is positively charged due to the presence of arginine and histidine residues (Figure
125 3B, E). However, pocket C is relatively superficial compared to the other pockets. No
126 density corresponding to bicarbonate is observed in these pockets (A–C), indicating that
127 they are not ligand binding sites. Nonetheless, they may serve as potential binding sites
128 for allosteric modulators or agonist drugs targeting GPR30.
129 Pocket D consists of ECL1–3 and TM2–7, and is the largest among the four
130 pockets. Although the surface of pocket D is partitioned by the C130$^{3.25}$-C207$^{45.52}$
131 disulfide bond and F208^{ECL2}, it is connected inside the receptor, deep enough to reach
132 W272$^{6.48}$. Pocket D contains numerous hydrophilic residues such as aspartate, glutamate,
133 asparagine, and glutamine, which favor bicarbonate binding, suggesting that pocket D is
134 a good candidate for the bicarbonate binding site.
135

136 **Insights into bicarbonate binding**

137 To predict the bicarbonate binding site, we performed an exhaustive mutant
138 analysis of hydrophilic residues in pockets A–D, which was not done in the previous
139 study[7]. We confirmed the similar expression levels of the HA-tagged hGPR30 mutants

140 by western blotting (Figure 4—figure supplement 1A, B). To evaluate the bicarbonate-
141 induced activation of GPR30, we used the TGFα shedding assay[23]. The HA-tagged
142 GPR30 wild-type showed a bicarbonate-dependent response, while the H307$^{7.36}$A mutant
143 completely abolished the response, consistent with previous findings [7](Figure 4A, B).
144 These results indicate that the present experimental procedure is useful to evaluate the
145 bicarbonate-induced activation of GPR30. Furthermore, the C207^{ECL2}A mutation that
146 disrupts the disulfide bond between ECL2 and ECL1, and the P71$^{1.44}$ mutant that disrupts
147 the characteristic kink in TM1, also abolished the bicarbonate response. These findings
148 underscore the critical role of the structural integrity of the receptor, and provide
149 compelling evidence that the bicarbonate response is mediated through GPR30.

150 Among the hydrophilic residue mutants, the alanine mutants of D125^{ECL1},
151 S134$^{3.29}$, D210^{ECL2}, and Q215$^{5.39}$ reduced the bicarbonate response (Figure 4A, B).
152 Combining these data with previous studies, we mapped the residues essential for the
153 bicarbonate response on the current structure (P71$^{1.44}$, E115$^{2.60}$, D125^{ECL1}. S134$^{3.29}$,
154 Q138$^{3.33}$, C207^{ECL2}, D210^{ECL2}, Q215$^{5.39}$, and H307$^{7.36}$) (Figure 4C). Except for the
155 structure-contributing residues (C207^{ECL2}and P71$^{1.44}$) and H307$^{7.36}$, the essential residues
156 face pocket D, further supporting its role as the bicarbonate binding site. H307$^{7.36}$
157 separates pockets A and B (Figure 3C), and the nearby mutants Q296$^{7.25}$ and N310$^{7.39}$ had
158 no effect on the bicarbonate response, suggesting the indirect importance of stabilizing
159 the active conformation of the receptor, rather than directly binding to bicarbonate.

160 Given the low affinity of GPR30 for bicarbonate[7] and the challenges posed by
161 carboxylic acid decarboxylation in cryo-EM analysis, visualizing bicarbonate at this
162 resolution could be difficult. Nevertheless, we observed a weak density in pocket D,
163 allowing us to assign bicarbonate (Figure 4D). The bicarbonate is surrounded by Q138$^{3.33}$,
164 Q215$^{5.39}$, and E218$^{5.42}$ (Figure 4E). Q138$^{3.33}$ and Q215$^{5.39}$ are residues with reduced
165 bicarbonate responses due to mutations (Figure 4C). Most bicarbonate binding modes in
166 other structures require recognition by asparagine and glutamine residues, in agreement
167 with our model. Moreover, Q138$^{3.33}$, Q215$^{5.39}$, and E218$^{5.42}$ are evolutionarily conserved
168 in fish to human GPR30s（Figure 4—figure supplement 2). Below the bicarbonate
169 binding site, M141$^{3.36}$ forms a hydrophobic interaction with W272$^{6.48}$ (Figure 4D), a
170 toggle switch motif essential for receptor activation[21,24]. These observations allowed us

171 to speculate that bicarbonate binding induces conformational changes in TM3 and TM5,
172 facilitating receptor activation.
173
174 **G-protein coupling**

175 The C-terminal helix of $G\alpha_q$ (α5-helix) is deeply enters the intracellular cavity of
176 GPR30, resulting in the formation of an active signaling complex. On the C-terminal side
177 of the α5-helix, the backbone carbonyl of $Y243^{G.H5.23}$ (superscript indicates the common
178 Gα numbering [CGN] system[25]) hydrogen bonds with $R155^{3.50}$ in the conserved
179 $D^{3.49}R^{3.50}Y^{3.51}$ motif[21] (Figure 5A). In addition, $N244^{G.H5.24}$ forms hydrogen bonds with
180 the peptide backbones of $Y324^{7.53}$ and $F331^{8.50}$. ICL3 faces the middle part of the α5-
181 helix, with three characteristic arginine residues ($R248^{6.24}$, $R251^{6.27}$, and $R254^{6.30}$)
182 surrounding $D233^{G.H5.13}$ (Figure 5B). $R248^{6.24}$ and $R254^{6.27}$ form hydrogen bonds with
183 $D233^{G.H.13}$ and $Q237^{G.H5.17}$, respectively. Moreover, $R251^{6.30}$ extends toward the G-
184 protein and hydrogen bonds with the peptide backbones of $G207^{G.h4s6.11}$ and $H209^{G.h4s6.13}$.
185 At ICL2, $M163^{34.51}$ fits into a hydrophobic pocket composed of the α5-helix, the αN-β2
186 loop, and the β2-β3 loop of the Gα subunit, as in other GPCR-G_q complexes[26–30] (Figure
187 5C–H). Above it, $L159^{3.54}$ and $A162^{34.50}$ form extensive hydrophobic interactions with
188 $L235^{G.H5.15}$, $L236^{G.H5.16}$, and $L240^{G.H5.20}$ in the α5-helix. These tight interactions with the
189 α5-helix would enable the coupling of GPR30 with G_q.

190 The position of the α5-helix aligns with those in other GPCR-G_q complexes, but
191 the position of the αN-helix is rotated away from the receptor (Figure 5I). The
192 superimposition of the Gα subunits indicates that the rotation is not due to the movement
193 of the entire G protein, but rather a 33° bend in the αN-helix (Figure 5J). This is attributed
194 to variations in the interactions of the αN-helix with its receptors. The αN-helix interacts
195 with the intracellular ends of ICL2 and TM4 in receptor-specific modes. In most G_q-
196 coupled structures, ICL2 adopts an α-helix and $R^{34.55}$ interacts with $R38^{G.hns1.03}$ at the end
197 of the αN-helix. A typical example is the head-to-toe interaction between $R185^{34.55}$ and
198 $R32^{G.hns1.03}$ in the serotonin 5-HT_{2A} receptor[29] (Figure 5E). However, in GPR30, ICL2
199 does not adopt an α-helix and $R^{34.55}$ is replaced by $L167^{34.55}$, which displaces $R32^{G.hns1.03}$
200 downward through their interaction. Moreover, $T170^{34.58}$ and $R169^{34.57}$ form direct

201 hydrogen bonds with R31$^{G.hns1.02}$ and Y243$^{G.H5.23}$, respectively, which are not observed in
202 other GPCR-G_q complexes. We hypothesize that these interactions may underpin the
203 distinct αN rotation: A similar interaction between R38$^{G.hns1.03}$ and L136$^{34.54}$ is also
204 observed in histamine H1 receptor (H_1R)[26] (Figure 5D), in which translational rather than
205 rotational motion of αN is observed (Figure 5J).

206 Discussion

207 Our study has elucidated the distinctive structure of GPR30, characterized by the
208 kink of TM1 and the presence of multiple extracellular pockets formed by ECLs.
209 Structural analysis and unbiased mutagenesis experiments on hydrophilic residues
210 highlighted the largest pocket, designated as pocket D, as pivotal for bicarbonate
211 recognition. Through putative bicarbonate modeling, we have proposed the binding mode
212 of bicarbonate ions and the receptor activation mechanism. Overall, the elucidated
213 structure of the extracellular domain of GPR30 and the insights into bicarbonate binding
214 could facilitate the development of high-affinity drugs targeting GPR30.

215 It should be noted that our current model cannot fully explain all the mutagenesis
216 results, such as those involving E115$^{2.60}$, D125^{ECL1}. and D210$^{ECL2\ 7}$. Although negatively
217 charged residues generally repel bicarbonate, some structures have indicated their
218 involvement in bicarbonate recognition[31–34]. Thus, it is conceivable that these residues are
219 transiently involved in bicarbonate binding, or two bicarbonate molecules might be
220 accommodated within pocket D of GPR30. Future studies should focus on higher-
221 resolution structures and approaches such as using bicarbonate derivatives to further
222 evaluate bicarbonate binding.

223 GPR30 exhibits low homology to other GPCRs, with even closely related
224 receptors sharing less than 30% sequence identity. A BLAST analysis revealed that
225 GPR30 shares the highest sequence identity of 28% with the type 2 angiotensin II receptor
226 (AT_2R) (Figure 6—figure supplement 1). Consequently, we compared the current
227 structure of GPR30 with the ligand-bound AT_2R[35]. The superimposition of GPR30 and
228 AT_2R, with a Cα R.M.S.D. of 2.17 Å, suggests significant structural divergence between

229 the two (Figure 6A). Notably, there is no structural commonality between GPR30 and
230 AT2R in terms of the orientations of their respective TMs. Specifically, the extracellular
231 half of TM1 in GPR30 extends outward, and is kinked at $P71^{1.44}$ in the center of TM1
232 (Figure 6B). Near $P71^{1.44}$, $Y65^{1.38}$ and $F70^{1.43}$ are oriented towards the interior of the
233 receptor, forming hydrophobic interactions with $L113^{2.58}$ and $L331^{7.40}$ to stabilize the kink.
234 In the examination of the loops, ECL2 of AT_2R features a short β-sheet commonly found
235 in peptide-activated class A GPCRs[36–38], whereas that of GPR30 adopts an elongated
236 conformation that covers the extracellular pocket essential for the bicarbonate response
237 (Figure 4A, B). These comparisons underscore the unique structural characteristics of
238 GPR30.

239 In most GPCRs, TM1 forms a straight α-helix and is positioned away from the
240 orthosteric pocket formed by TM2–7. However, TM1 undergoes an inward movement
241 due to allosteric conformational changes during agonist binding. The cannabinoid
242 receptor CB_1 exemplifies this, with TM1 kinked at $G127^{1.43}$ and folding inward upon
243 ligand binding [39,40](Figure 6C). Similarly, the β_2 adrenergic receptor (β_2AR)[41,42] and
244 adenosine A2A receptor ($A_{2A}R$)[43,44] exhibit inward movements of TM1, with TM1
245 bending at the glycine residues rather than kinking (Figure 6D, E). By contrast, TM1
246 [24,45]moves 4 Å outward in the endothelin ET_B receptor (Figure 6F). In GPR30, TM1 is
247 kinked at $P71^{1.44}$ (Figure 6B), indicating that this kink occurs regardless of the receptor
248 activation state. Indeed, the $P71^{1.44}A$ mutation, which eliminates the kink in TM1,
249 completely abolished the bicarbonate response (Figure 4A, B). Moreover, $P71^{1.44}$ is
250 evolutionarily preserved (Figure 4—figure supplement 2). These findings suggest the
251 critical role of the TM1 kink in both the putative conformational changes associated with
252 ligand binding and the functional integrity of GPR30.

253

254 **Table. 1 Cryo-EM data collection, refinement and validation**
255 **statistics**

256

Data collection	GPR30-G_q complex

Microscope	Titan Krios (Thermo Fisher Scientific)
Voltage (keV)	300
Electron exposure (e^-/Å^2)	50.660
Detector	Gatan K3 Summit camera (Gatan)
Magnification	×105,000
Defocus range (μm)	-0.8–1.6
Pixel size (Å/pix)	0.83
Number of movies	9,824
Symmetry	C1
Picked particles	11,176,478
Final particles	148,285
Map resolution (Å)	3.21
FSC threshold	0.143
Model refinement	
Atoms	
R.m.s. deviations from ideal	
Bond lengths (Å)	0.004
Bond angles (°)	0.633
Validation	
Clashscore	9.17
Rotamers Outliers(%)	0.34
Ramachandran plot	
Favored (%)	93.77
Allowed (%)	6.23
Outlier (%)	0

259 # Figures

260 **Figure 1. Overall structure of the GPR30-miniG$_{sqi}$β$_1$γ$_2$-scFv16 complex.**

261 **A** Unsharpened cryo-EM density map of the GPR30-miniG$_{sqi}$β$_1$γ$_2$-scFv16-Nb35 complex,
262 with the components individually colored. **B** The refined structure of the complex is
263 shown as a ribbon representation.

264 **Figure 2. Receptor structure.**

265 **A–C** Overall structure of the receptor, viewed from the membrane plane (**A**), intracellular
266 side (**B**), and extracellular side (**C**). **D** Extracellular view of the ribbon model overlaid
267 the cryo-EM map.

268 **Figure 3. Architecture of the extracellular pocket.**

269 **A** Interactions between the ECLs. Black dashed lines indicate hydrogen bonds. **B**
270 Molecular surface of the extracellular side. **C**–**F** Residues facing pocket A (**C**), pocket B
271 (**D**), pocket C (**E**), and pocket D (**F**).

272 **Figure 4. Mutational analysis.**

273 **A, B** TGFα shedding assay using HEK293 cells transfected with HA-tagged hGPR30.
274 The mutants D111A; C207A, P71A, H307A; and D125A, S134A, D210A, Q215A are
275 highlighted in red, blue, and purple, respectively. Statistical analysis: $^{\$}$ $p = 0.0001$, $^{\#}$ p
276 < 0.0001 compared to mock cells using two-tailed unpaired t-test with Bonferroni's
277 correction after two-way ANOVA. ns indicates no significant difference. Data are
278 presented as mean values (**A**) and mean values ± SEM (**B**). **C** Residues that were
279 subjected to mutant analysis are mapped to the structure. Only residues with reduced
280 bicarbonate responses are colored.in magenta. **D** Density corresponding to bicarbonate.
281 **E** Putative binding mode of bicarbonate. Black dashed lines indicate hydrogen bonds.

282 **Figure 5. G-protein coupling.**

283 **A** Hydrogen-bonding interactions between the C-terminal α5-helix residues and the

284 receptor. **B** Electrostatic and hydrogen-binding interactions between ICL3 and the α5-
285 helix. **C–H** Interface between ICL2 and G_q, with residues involved in hydrophobic
286 interactions represented by CPK models. G-protein-bound GPCRs used in the
287 comparison are as follows: H_1R-G_q (PDB 7DFL, gray), B_2R-G_q (PDB 7F6I, yellow-
288 green), $MRGPRX_2$-G_q (PDB 7S8L, green), 5-HT_{2A}-G_q (PDB 6WHA, gray), and
289 GPR103-G_q (PDB 8ZH8, red). **I** Comparison of the angles and positions of α5h and αN
290 relative to the receptor. **J** Superimposition of the Gα subunits.

291 **Figure 6. Structural comparison with related GPCRS.**

292 **A** Structural comparison of GPR30 and AT_2R (PDB 5UNF). **B** Interactions around P70
293 in TM1 of GPR30. **C–F** Conformational changes of TM1 upon agonist binding in CB1
294 (**C**), β_2AR (**D**), $A_{2A}R$ (**E**), and ET_B (**F**). The agonist-bound states are colored with the
295 respective colors, while the inactive states are colored gray. The PDB codes used in this
296 figure are CB1-active (PDB 5XRA), CB_1-inactive (PDB 5TGZ), β_2AR-active (PDB
297 3SN6), β_2AR-inactive (PDB 2RH1), $A_{2A}R$-active(PDB 6GDG), $A_{2A}R$-inactive (PDB
298 3EML), ET_B-active (PDB 8IY5), and ET_B-inactive (PDB 5X93).

299 **Figure 1.—figure supplement 1.** Sample purification.
300 **A** Schematic representation of the fusion-G system. **B** Fluorescence-detection size-
301 exclusion chromatography (FSEC) analysis of complex formation by GPR30. Solubilized
302 cells expressing only GPR30 are orange, and those co-expressing GPR30 and G-protein
303 are blue. **C** Size-exclusion chromatography of the GPR30-G-protein complex on a
304 Superose 6 Increase column. The fraction shaded in blue was collected. **D** SDS-PAGE
305 gel of samples after size-exclusion chromatography, stained with Coomassie Brilliant
306 Blue.
307
308 **Figure 1.—figure supplement 2.** Cryo-EM analysis.
309 Flow chart of the cryo-EM data processing for the GPR30-G_q complex, including particle
310 projection selection, classification, and 3D density map reconstruction. The 3D density
311 map was refined with a mask on the receptor. Details are provided in the Methods section.
312

Figure 3.—figure supplement 1. Structural comparison with AlphaFold-predicted structure.

A–C Superimposition of the cryo-EM (orange) and AF2 (khaki) structures. (**A**) Overall view of the receptor, (**B**) focused on the intracellular side, and (**C**) focused on the extracellular side.

Figure 4.—figure supplement 1. Cell surface expression of mutant receptors.

A Whole cell expression of HA-tagged mutants, analyzed by western blotting. **B** Cell surface expression of HA-tagged mutants, using cell surface biotinylation and avidin immunoprecipitation, analyzed by western blotting.

Figure 4.—figure supplement 2. Conservation of the GPR30 homologs.

Amino acid alignment of representative GPR30 homologs.

Figure 6.—figure supplement 1. Sequence alignment of GPR30 and AT_2R.

Data Availability

The cryo-EM density map and atomic coordinates for the LPA_1-G_i complex have been deposited in the Electron Microscopy Data Bank and the PDB, under the accession codes: EMD-XXXXX [https://www.ebi.ac.uk/emdb/entry/EMD-XXXXX], and PDB XXXX [http://doi.org/10.2210/pdbXXXX/pdb]. Source data are provided with this paper. All other data are available from the corresponding authors upon reasonable request.

Acknowledgements

We thank K. Ogomori and C. Harada for technical assistance. This work was supported by grants from the JSPS KAKENHI, grant numbers 21H05037 (O.N.), 22K19371 and 22H02751 (W.S.), 23K06393 (A.J-W.); the Japan Agency for Medical Research and Development (AMED), Innovation and Clinical Research Center Project, PRIME, grant number JP20gm6210026 (A.J.-W.); the JST FOREST Program (Grant

342 number JPMJFR220S to A.J.-W.); the Takeda Science Foundation (W.S.); the Lotte
343 Foundation (W.S.); AMED, grant number JP233fa627001 (O.N.); and the Platform
344 Project for Supporting Drug Discovery and Life Science Research (Basis for Supporting
345 Innovative Drug Discovery and Life Science Research (BINDS)) from AMED, grant
346 numbers JP23ma121002 (support number 3272, O.N.) and JP23ama121012 (supporting
347 number 4869, T.Y.).
348

349 ## Author contributions

350 S.K. performed all the experiments involved in the structural determination,
351 assisted by H.A. and H.S.O. W.S. designed the project and initially tried the expression
352 of GPR30. A.J.-W. and T.Y. performed and oversaw the mutagenesis study. The
353 manuscript was mainly prepared by S.K. and W.S., with assistance from O.N.
354

355 ## Competing interests

356 O.N. is a co-founder and scientific advisor for Curreio. All other authors declare
357 no competing interests.

358 # Methods

359 **Expression and purification of scFv16 and Nb35**

360 The gene encoding scFv16 was synthesized (GeneArt) and subcloned into a
361 modified pFastBac vector[46], with the resulting construct encoding the GP67 secretion
362 signal sequence at the N terminus, and a His_8 tag followed by a TEV cleavage site at the
363 C terminus. The His_8-tagged scFv16 was expressed and secreted by Sf9 insect cells, as
364 previously reported[44]. The Sf9 cells were removed by centrifugation at 5,000g for 10 min,
365 and the secreta-containing supernatant was combined with 5 mM $CaCl_2$, 1 mM $NiCl_2$,
366 20 mM HEPES (pH 8.0), and 150 mM NaCl. The supernatant was mixed with Ni
367 Superflow resin (GE Healthcare Life Sciences) and stirred for 1 h at 4 °C. The collected

368 resin was washed with buffer containing 20 mM HEPES (pH 8.0), 500 mM NaCl and
369 20 mM imidazole, and further washed with 10 column volumes of buffer containing
370 20 mM HEPES (pH 8.0), 500 mM NaCl and 20 mM imidazole. Next, the protein was
371 eluted with 20 mM Tris (pH 8.0), 500 mM NaCl and 400 mM imidazole. The eluted
372 fraction was concentrated and loaded onto a Superdex200 10/300 Increase size-exclusion
373 column, equilibrated in buffer containing 20 mM Tris (pH 8.0) and 150 mM NaCl. Peak
374 fractions were pooled, concentrated to 5 mg/ml using a centrifugal filter device (Millipore
375 10 kDa MW cutoff), and frozen in liquid nitrogen.
376 Nb35 was prepared as previously reported[47,48]. In brief, Nb35 was expressed in
377 the periplasm of *E. coli*. The harvested cells were disrupted by sonication. Nb35 was
378 purified by nickel affinity chromatography, followed by gel-filtration chromatography,
379 and frozen in liquid nitrogen.
380
381 **Constructs for expression of GPR30 and G_q**

382 The human GPR30 gene (UniProtKB, Q99527) was subcloned into a modified
383 pFastBac vector[49], with an N-terminal haemagglutinin signal peptide followed by the
384 Flag-tag epitope (DYKDDDDK) and the LgBiT fused to its C-terminus followed by a 3
385 C protease site and EGFP-His_8 tag. A 15 amino sequence of GGSGGGGSGGSSSGG was
386 inserted into both the N-terminal and C-terminal sides of LgBiT. Rat $G\beta_1$ and bovine $G\gamma_2$
387 were subcloned into the pFastBac Dual vector. In detail, rat $G\beta_1$ was cloned with a C-
388 terminal HiBiT connected with a 15 amino sequence of GGSGGGGSGGSSSGG.
389 Moreover, mini-G_{sqi} was subcloned into the C-terminus of the bovine $G\gamma_2$ with a nine
390 amino sequence GSAGSAGSA linker. The resulting pFastBac dual vector can express
391 the mini-G_{sqi} trimer.
392
393 **Expression and purification of the human GPR30 – G_q complex**

394 The recombinant baculovirus was prepared using the Bac-to-Bac baculovirus
395 expression system (Thermo Fisher Scientific). For expression, 2 L of Sf9 cells at a density
396 of 3×10^6 cells/mL were co-infected with baculovirus encoding GPR30 and miniGsqi
397 trimer at the ratio of 1:1 and the cells were incubated at 30°C. After 48 hours, the collected

398 cells were resuspended and dounce-homogenized in 20 mM Tris-HCl, pH 8.0(4°C),
399 200 mM NaCl, 10% Glycerol, 200 mM $NaHCO_3$, 25 mU/ml apyrase. The crude
400 membrane fraction was collected by ultracentrifugation at 180,000*g* for 1 h and
401 solubilized in buffer, containing 20 mM Tris-HCl, pH 8.0, 150 mM NaCl, 1% n-dodecyl-
402 beta-D-maltopyranoside (DDM) (Calbiochem), 0.2 % cholesteryl hemisuccinate (CHS)
403 (Merck), 10% glycerol, 200 mM $NaHCO_3$, and 25 mU/ml Apyrase, for 1 h at 4 °C. The
404 supernatant was separated from the insoluble material by ultracentrifugation at 180,000*g*
405 for 20 min and incubated with 5 mL of Anti-DYKDDDDK M2 resin (Sigma) for 1 h at
406 4°C. The resin was washed with 20 column volumes of buffer containing 20 mM Tris-
407 HCl, pH 8.0 500 mM NaCl, 10% Glycerol, 0.05% Lauryl Maltose Neopentyl Glycol
408 (LMNG) (Antrace), 0.005% CHS and 200 mM $NaHCO_3$. The complex was eluted in
409 buffer containing 20 mM Tris-HCl, pH 8.0, 150 mM NaCl, 10% Glycerol, 0.01% LMNG,
410 0.001% CHS, 200 mM $NaHCO_3$ and 0.2 mg/mL Flag peptide. The eluate was incubated
411 with the Nb35 and scFv16 at 4 °C. The complex was concentrated and purified by size
412 exclusion chromatography on a Superose 6 increase (GE) column in 20 mM Tris-HCl,
413 pH8.0, 150 mM NaCl, 0.01% LMNG, 0.001% CHS and 200 mM $NaHCO_3$. Peak fractions
414 were concentrated to 4.72 mg/ml for electron microscopy studies.
415

416 **Sample vitrification and cryo-EM data acquisition**

417 The purified complex was applied onto a freshly glow-discharged
418 Quantifoil UltraAu grid (R1.2/1.3, 300 mesh), and plunge-frozen in liquid ethane by
419 using a Vitrobot Mark IV. Data collections were performed on a 300kV Titan Krios G3i
420 microscope (Thermo Fisher Scientific) equipped with a BioQuantum K3 imaging filter
421 and a K3 direct electron detector (Gatan).
422 A total of 9824 movies were acquired with a calibrated pixel size of 0.83 Å pix^{-1}
423 and with a defocus range of -0.8 to -1.6 µm, using EPU. Each movie was acquired for
424 2.6 s and split into 48 frames, resulting in an accumulated exposure of about
425 50.660 electrons per $Å^2$.
426

427 **Image processing**

428 All acquired dose-fractionated movies were imported into CryoSPARC v4.4[50] and
429 subjected to beam-induced motion correction. The contrast transfer function (CTF)
430 parameters were estimated and a total of 10,148,422 particles were extracted. The
431 particles were subjected to 2D classifications, Ab-initio reconstruction and several rounds
432 of hetero refinement and Non-uniform refinement. Next, the particles were subjected to
433 3D classification with a mask on the receptor. Then the particle sets were subjected to
434 Reference Based Motion Correction. Motion-corrected 148,285 particles were subjected
435 to Non-uniform refinement, yielding a map with a global nominal resolution of 3.21 Å,
436 with the gold standard Fourier Shell Correlation (FSC=0.143) criteria[51]. Moreover, the
437 3D model was refined with a mask on the receptor. As a result, the receptor has a higher
438 resolution with a nominal resolution of 3.30 Å. The overall and receptor focused maps
439 were combined by phenix[52]. The processing strategy is described in Supplementary
440 Figure 2.
441

442 **Model building and refinement**

443 The density map was sharpened by phenix.auto_sharpen[53] and the quality of the
444 density map was sufficient to build a model manually in COOT[54,55]. The model building
445 was facilitated by the Alphafold-predicted structure. We manually fitted GPR30, the
446 G_q heterotrimer and scFv16 into the map. We then manually readjusted the model into
447 using COOT and refined it using phenix.real_space_refine[52,56] (v.1.19) with the
448 secondary-structure restraints using phenix secondary_structure_restraints.
449

450 **Vector construction and transfection**

451 Human *Gpr30* cDNA was obtained from human hepatoblastoma-derived HepG2 cells.
452 The coding sequences of human *Gpr30* were inserted into the multi-cloning site of the
453 plasmid vector pCXN2, which was generated in our laboratory via modification of
454 pCAGGS, between the KpnI and EcoRI sites. The C-terminal HA-tagged *Gpr30* was
455 amplified using a reverse primer containing the HA sequenceOne amino acid mutation

456 of human GPR30 was generated as follows: the targeted amino acid was changed to
457 alanine (GCC) using a two-step PCR method with the QuikChange® Primer Design
458 Program by Agilent (https://www.agilent.com/store/primerDesignProgram.jsp), and the
459 coding sequence with each mutation was inserted into the multi-cloning site of pCXN2
460 between the KpnI and EcoRI sites. The mutations generated were D111A, E121A, R122A,
461 D125A, S134A, D210A, Q215A, N276A, Q296A, C207A, P71A, and H307A.

462 **Cell line sources and transfection**

463 HEK293A cells (female origin; Thermo Fisher Scientific) were maintained at 37 °C and
464 5% CO_2. These vectors were transfected using the lipofection method (Lipofectamine™
465 2000 Transfection Reagent, 11668019, Invitrogen).

466 **TGFα shedding assay**

467 The TGFα shedding assay was performed according to a previously published protocol[23].
468 AP-TGFα expression vector was provided by Dr. Inoue and Dr. Aoki, Tohoku University.
469 HEK293 cells were seeded in 12-well plates at a density of 1×10^5 cells/well and cultured
470 for 24 h. At 70% confluency, a mixture of plasmid vectors containing GPCR (see '***Vector***
471 ***construction and transfection***' section) and AP-TGFα was transfected into the cells using
472 Lipofectamine 2000 transfection reagent. After another 24 h of incubation, the cells were
473 detached with 0.05% trypsin/EDTA (32777-44, Nacalai Tesque), suspended in Hanks'
474 balanced salt solution, and seeded in 96-well plates. The cells were stimulated for 1 h
475 with $1–44\times10^{-3}$ M (final concentration) of $NaHCO_3$ at 37 °C, under 0.03% CO_2.
476 Conditioned media (CM) was transferred to another plate, and 80 μl of alkaline
477 phosphatase (AP) solution (40 mM Tris-HCl, pH 9.5, 40 mM NaCl, 10 mM $MgCl_2$, 10
478 mM p-nitrophenylphosphate disodium salt hexahydrate) was added to both plates, which
479 were then incubated at 37 °C. The optical density at 405 nm (OD405) was measured using
480 a microplate reader (iMark, Bio-Rad) at 5 min, 30 min, 1 h, and 2 h, depending on the
481 reaction rate. The percentage of shed AP-TGF was calculated using the following
482 equations:

483 $$\text{AP activity} = \Delta OD405\ (1 - 0\ h)$$

484 % CM (conditioned media) = AP_{CM} / (AP_{CM} + AP_{Cell})

485 [15]**Analysis of cell surface expression of GPR30**

486 The cell surface expression of wild-type and mutant hGPR30-HA was analysed via cell
487 surface protein isolation using a Cell Surface Protein Isolation Kit (#89881, Thermo
488 Scientific™) followed by western blotting. Briefly, HEK293 cells transiently expressing
489 wild-type or mutant hGPR30-HA were biotinylated for 30 min at 4 °C. Then, the cells
490 were harvested, and biotinylated proteins were isolated with avidin binding.

491 **Western blotting**

492 Cell lysates were separated using sodium dodecyl sulfate-polyacrylamide gel
493 electrophoresis under reducing conditions and transferred to polyvinylidene difluoride
494 membranes (Immobilon P, IPVH00010, Millipore). Primary antibodies used were anti-
495 HA High Affinity, 1:1000 dilution, 11867423001, Roche; Na-K-ATPase, 1:1000 dilution,
496 #3010, Cell Signaling Technology; β-Actin (AC-15), 1:1000 dilution, sc-69879, Santa
497 Cruz Biotechnology. Secondary antibodies used were anti-rabbit IgG, HRP-linked
498 Antibody, 1:5000 dilution, #7074, Cell Signaling Technology; anti-mouse IgG, HRP-
499 linked Antibody, 1:5000 dilution, #7076, Cell Signaling Technology; anti-rat IgG, HRP-
500 Linked Whole Ab Goat, 1:5000 dilution, NA935, Cytiva. The membranes were probed at
501 4 °C overnight with the primary antibodies. The membranes were subsequently incubated
502 with the corresponding secondary antibodies. The signals were detected with ECL Prime
503 (RPN2236, Cytiva) or ImmunoStar LD (296-69901, FUJIFILM Wako Pure Chemical
504 Corporation) using a chemiluminescence imaging system (CFusion FX7, Vilber).

505

506

507 1. Brinkman, J. E. & Sharma, S. Physiology, Metabolic Alkalosis. in *StatPearls*
508 (StatPearls Publishing, Treasure Island (FL), 2024).
509 2. Ludwig, M.-G. *et al.* Proton-sensing G-protein-coupled receptors. *Nature* **425**, 93–98
510 (2003).

511 3. Murakami, N., Yokomizo, T., Okuno, T. & Shimizu, T. G2A is a proton-sensing G-
512 protein-coupled receptor antagonized by lysophosphatidylcholine. *J Biol Chem* **279**,
513 42484–42491 (2004).
514 4. Wang, J.-Q. *et al.* TDAG8 is a proton-sensing and psychosine-sensitive G-protein-
515 coupled receptor. *J Biol Chem* **279**, 45626–45633 (2004).
516 5. Wang, J.-L. *et al.* Functional screening and rational design of compounds targeting
517 GPR132 to treat diabetes. *Nat Metab* **5**, 1726–1746 (2023).
518 6. Imenez Silva, P. H., Camara, N. O. & Wagner, C. A. Role of proton-activated G
519 protein-coupled receptors in pathophysiology. *Am J Physiol Cell Physiol* **323**, C400–
520 C414 (2022).
521 7. Jo-Watanabe, A. *et al.* Bicarbonate signalling via G protein-coupled receptor
522 regulates ischaemia-reperfusion injury. *Nat Commun* **15**, 1530 (2024).
523 8. Revankar, C. M., Cimino, D. F., Sklar, L. A., Arterburn, J. B. & Prossnitz, E. R. A
524 transmembrane intracellular estrogen receptor mediates rapid cell signaling. *Science*
525 **307**, 1625–1630 (2005).
526 9. Ford, J. *et al.* GPR30 deficiency causes increased bone mass, mineralization, and
527 growth plate proliferative activity in male mice. *J Bone Miner Res* **26**, 298–307
528 (2011).
529 10. Sharma, G. *et al.* GPER deficiency in male mice results in insulin resistance,
530 dyslipidemia, and a proinflammatory state. *Endocrinology* **154**, 4136–4145 (2013).
531 11. Tutzauer, J. *et al.* Ligand-Independent G Protein-Coupled Estrogen Receptor/G
532 Protein-Coupled Receptor 30 Activity: Lack of Receptor-Dependent Effects of G-1
533 and 17β-Estradiol. *Mol Pharmacol* **100**, 271–282 (2021).

534 12. Lamprecht, M. R. & Morrison, B. GPR30 activation is neither necessary nor
535 sufficient for acute neuroprotection by 17β-estradiol after an ischemic injury in
536 organotypic hippocampal slice cultures. *Brain Res* **1563**, 131–137 (2014).
537 13. Otto, C. *et al.* GPR30 does not mediate estrogenic responses in reproductive organs
538 in mice. *Biol Reprod* **80**, 34–41 (2009).
539 14. Uhlén, M. *et al.* Proteomics. Tissue-based map of the human proteome. *Science* **347**,
540 1260419 (2015).
541 15. The Human Protein Atlas. https://www.proteinatlas.org/.
542 16. Vanlandewijck, M. *et al.* A molecular atlas of cell types and zonation in the brain
543 vasculature. *Nature* **554**, 475–480 (2018).
544 17. Winkler, E. A. *et al.* A single-cell atlas of the normal and malformed human brain
545 vasculature. *Science* **375**, eabi7377 (2022).
546 18. Kooistra, A. J. *et al.* GPCRdb in 2021: integrating GPCR sequence, structure and
547 function. *Nucleic Acids Res* **49**, D335–D343 (2021).
548 19. Sano, F. K., Akasaka, H., Shihoya, W. & Nureki, O. Cryo-EM structure of the
549 endothelin-1-ETB-Gi complex. *Elife* **12**, e85821 (2023).
550 20. Shihoya, W., Iwama, A., Sano, F. K. & Nureki, O. Cryo-EM advances in GPCR
551 structure determination. *J Biochem* mvae029 (2024) doi:10.1093/jb/mvae029.
552 21. Venkatakrishnan, A. J. *et al.* Molecular signatures of G-protein-coupled receptors.
553 *Nature* **494**, 185–194 (2013).
554 22. Ballesteros, J. A. & Weinstein, H. [19] Integrated methods for the construction of
555 three-dimensional models and computational probing of structure-function relations
556 in G protein-coupled receptors. in *Methods in Neurosciences* (ed. Sealfon, S. C.) vol.

557 25 366–428 (Academic Press, 1995).
558 23. Inoue, A. *et al.* TGFα shedding assay: an accurate and versatile method for detecting
559 GPCR activation. *Nat Methods* **9**, 1021–1029 (2012).
560 24. Shihoya, W., Sano, F. K. & Nureki, O. Structural insights into endothelin receptor
561 signalling. *J Biochem* **174**, 317–325 (2023).
562 25. Flock, T. *et al.* Universal allosteric mechanism for Gα activation by GPCRs. *Nature*
563 **524**, 173–179 (2015).
564 26. Xia, R. *et al.* Cryo-EM structure of the human histamine H1 receptor/Gq complex.
565 *Nat Commun* **12**, 2086 (2021).
566 27. Shen, J. *et al.* Cryo-EM structures of human bradykinin receptor-Gq proteins
567 complexes. *Nat Commun* **13**, 714 (2022).
568 28. Cao, C. *et al.* Structure, function and pharmacology of human itch GPCRs. *Nature*
569 **600**, 170–175 (2021).
570 29. Kim, K. *et al.* Structure of a Hallucinogen-Activated Gq-Coupled 5-HT2A Serotonin
571 Receptor. *Cell* **182**, 1574-1588.e19 (2020).
572 30. Iwama, A. *et al.* Structure and dynamics of the RF-amide QRFP receptor GPR103.
573 2023.12.06.570340 Preprint at https://doi.org/10.1101/2023.12.06.570340 (2023).
574 31. Capper, M. J. *et al.* Substrate binding and inhibition of the anion exchanger 1
575 transporter. *Nat Struct Mol Biol* **30**, 1495–1504 (2023).
576 32. Fang, S. *et al.* Molecular mechanism underlying transport and allosteric inhibition of
577 bicarbonate transporter SbtA. *Proc Natl Acad Sci U S A* **118**, e2101632118 (2021).
578 33. Koropatkin, N. M., Koppenaal, D. W., Pakrasi, H. B. & Smith, T. J. The structure of
579 a cyanobacterial bicarbonate transport protein, CmpA. *J Biol Chem* **282**, 2606–2614

580 (2007).
581 34. Wang, W. *et al.* Cryo-EM structure of the sodium-driven chloride/bicarbonate
582 exchanger NDCBE. *Nat Commun* **12**, 5690 (2021).
583 35. Zhang, H. *et al.* Structural basis for selectivity and diversity in angiotensin II
584 receptors. *Nature* **544**, 327–332 (2017).
585 36. Hong, C. *et al.* Structures of active-state orexin receptor 2 rationalize peptide and
586 small-molecule agonist recognition and receptor activation. *Nat Commun* **12**, 815
587 (2021).
588 37. Mobbs, J. I. *et al.* Structures of the human cholecystokinin 1 (CCK1) receptor bound
589 to Gs and Gq mimetic proteins provide insight into mechanisms of G protein
590 selectivity. *PLoS Biol* **19**, e3001295 (2021).
591 38. Tang, T. *et al.* Receptor-specific recognition of NPY peptides revealed by structures
592 of NPY receptors. *Sci Adv* **8**, eabm1232 (2022).
593 39. Hua, T. *et al.* Crystal structures of agonist-bound human cannabinoid receptor CB1.
594 *Nature* **547**, 468–471 (2017).
595 40. Hua, T. *et al.* Crystal Structure of the Human Cannabinoid Receptor CB1. *Cell* **167**,
596 750-762.e14 (2016).
597 41. Cherezov, V. *et al.* High-resolution crystal structure of an engineered human beta2-
598 adrenergic G protein-coupled receptor. *Science* **318**, 1258–1265 (2007).
599 42. Rasmussen, S. G. F. *et al.* Crystal structure of the β2 adrenergic receptor-Gs protein
600 complex. *Nature* **477**, 549–555 (2011).
601 43. García-Nafría, J., Lee, Y., Bai, X., Carpenter, B. & Tate, C. G. Cryo-EM structure of
602 the adenosine A2A receptor coupled to an engineered heterotrimeric G protein. *Elife*

603 **7**, e35946 (2018).
604 44. Jaakola, V.-P. *et al.* The 2.6 angstrom crystal structure of a human A2A adenosine
605 receptor bound to an antagonist. *Science* **322**, 1211–1217 (2008).
606 45. Shihoya, W. *et al.* Activation mechanism of endothelin ETB receptor by endothelin-
607 1. *Nature* **537**, 363–368 (2016).
608 46. Okamoto, H. H. *et al.* Cryo-EM structure of the human MT1-Gi signaling complex.
609 *Nat Struct Mol Biol* **28**, 694–701 (2021).
610 47. Nagiri, C. *et al.* Cryo-EM structure of the β3-adrenergic receptor reveals the
611 molecular basis of subtype selectivity. *Mol Cell* **81**, 3205-3215.e5 (2021).
612 48. Nureki, I. *et al.* Cryo-EM structures of the β3 adrenergic receptor bound to solabegron
613 and isoproterenol. *Biochem Biophys Res Commun* **611**, 158–164 (2022).
614 49. Sano, F. K., Akasaka, H., Shihoya, W. & Nureki, O. Cryo-EM structure of the
615 endothelin-1-ETB-Gi complex. *eLife* **12**, e85821 (2023).
616 50. Punjani, A., Rubinstein, J. L., Fleet, D. J. & Brubaker, M. A. cryoSPARC: algorithms
617 for rapid unsupervised cryo-EM structure determination. *Nat Methods* **14**, 290–296
618 (2017).
619 51. Rosenthal, P. B. & Henderson, R. Optimal determination of particle orientation,
620 absolute hand, and contrast loss in single-particle electron cryomicroscopy. *J Mol*
621 *Biol* **333**, 721–745 (2003).
622 52. Adams, P. D. *et al.* PHENIX: a comprehensive Python-based system for
623 macromolecular structure solution. *Acta Crystallogr D Biol Crystallogr* **66**, 213–221
624 (2010).
625 53. Terwilliger, T. C., Sobolev, O. V., Afonine, P. V. & Adams, P. D. Automated map

sharpening by maximization of detail and connectivity. *Acta Crystallogr D Struct Biol* **74**, 545–559 (2018).

54. Emsley, P. & Cowtan, K. Coot: model-building tools for molecular graphics. *Acta Crystallogr D Biol Crystallogr* **60**, 2126–2132 (2004).
55. Emsley, P., Lohkamp, B., Scott, W. G. & Cowtan, K. Features and development of Coot. *Acta Crystallogr D Biol Crystallogr* **66**, 486–501 (2010).
56. Afonine, P. V. *et al.* Real-space refinement in PHENIX for cryo-EM and crystallography. *Acta Crystallogr D Struct Biol* **74**, 531–544 (2018).

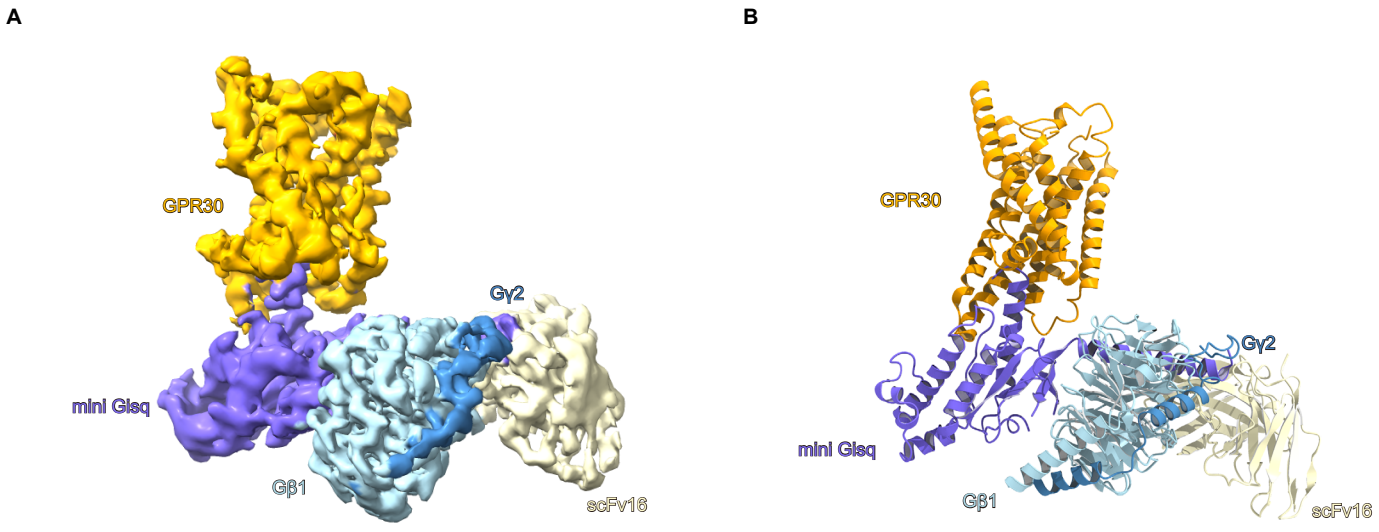

Figure 1. Overall structure of the GPR30-miniG$_{sqi}$β$_1$γ$_2$-scFv16 complex.
A Unsharpened cryo-EM density map of the GPR30-miniG$_{sqi}$β$_1$γ$_2$-scFv16-Nb35 complex, with the components individually colored. **B** The refined structure of the complex is shown as a ribbon representation.

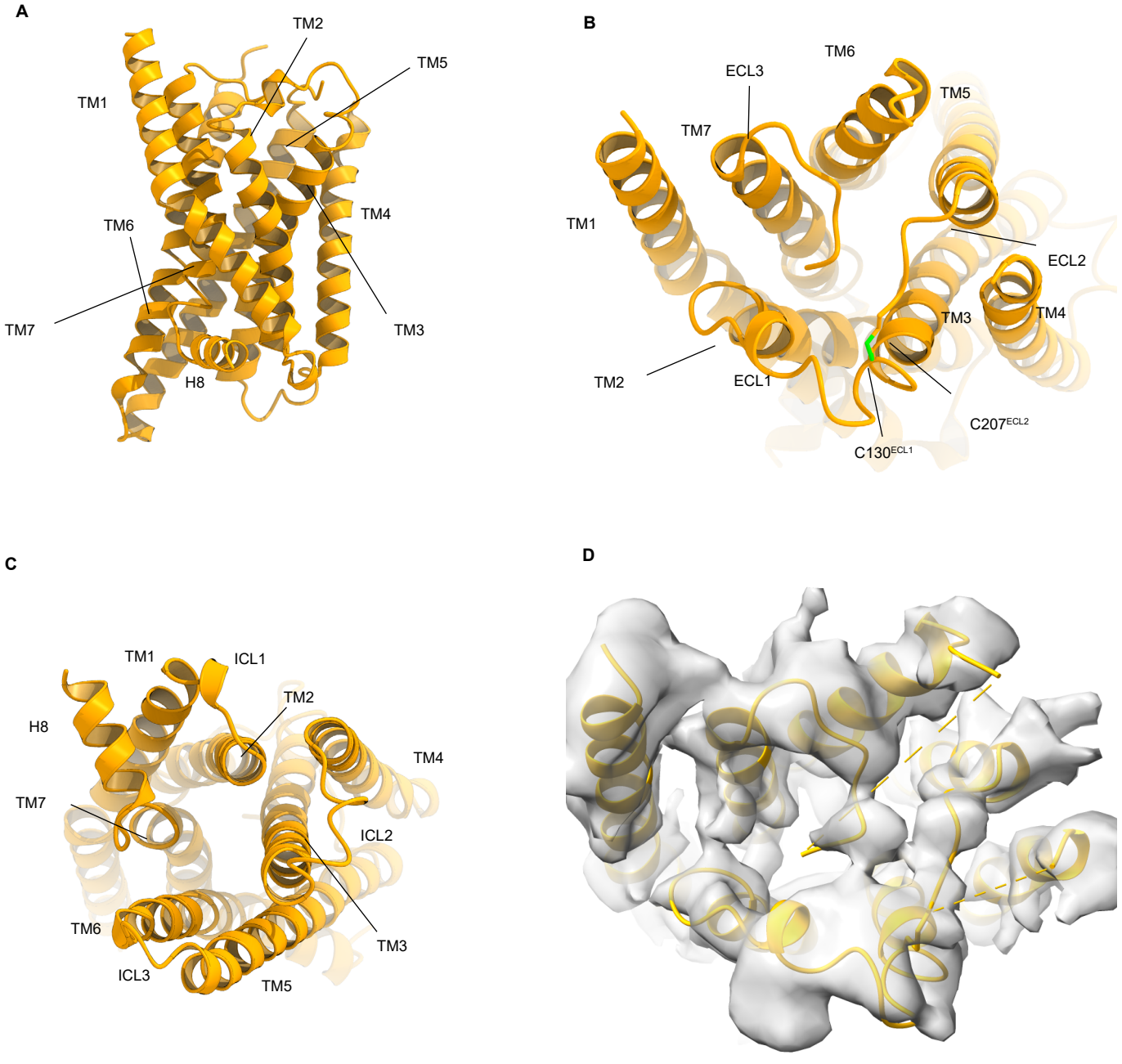

Figure 2. Receptor structure.
A–C Overall structure of the receptor, viewed from the membrane plane (**A**), extracellular side (**B**), and intracellular side (**C**).**D** Extracellular view of the ribbon model overlaid the cryo-EM map.

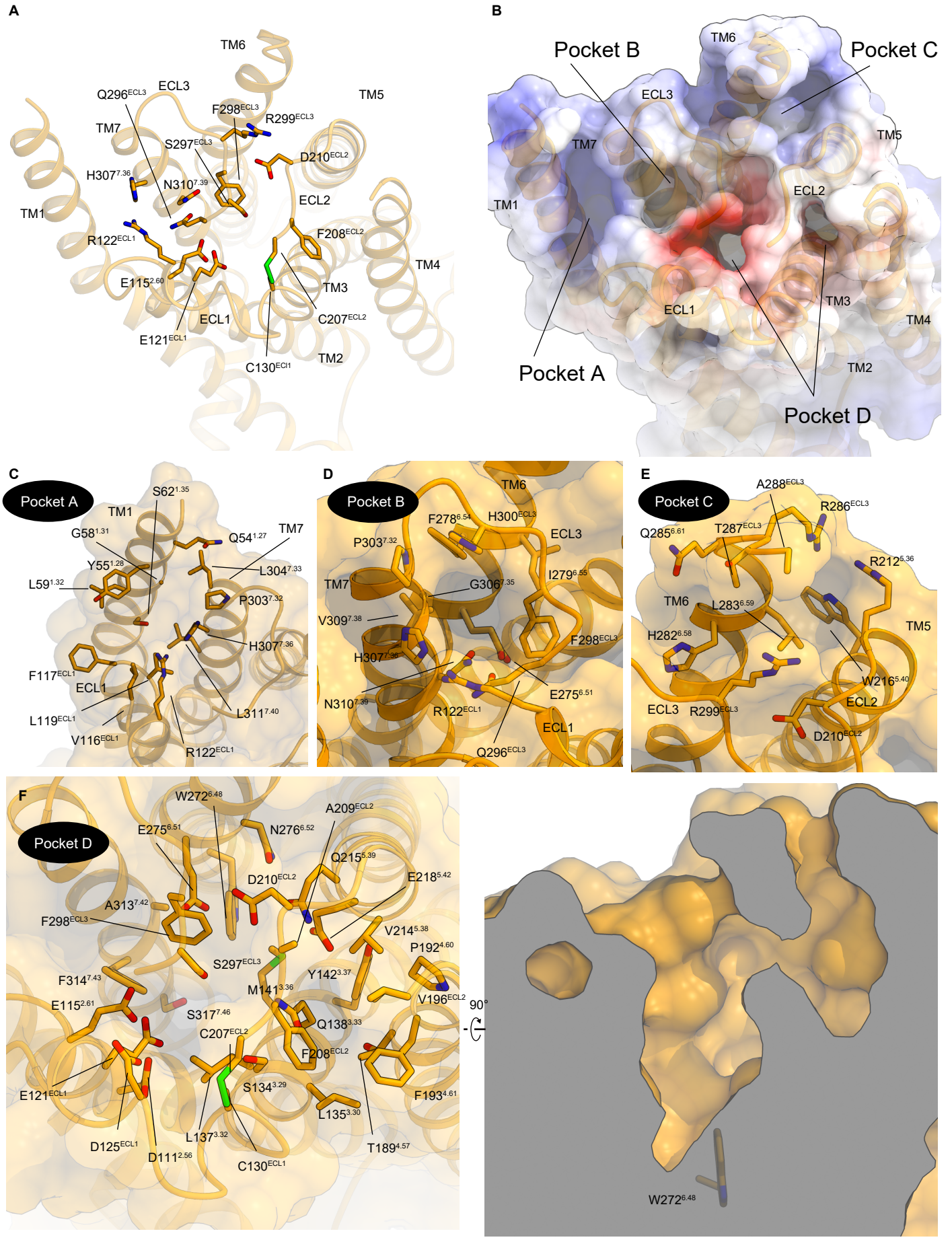

Figure 3. Architecture of the extracellular pocket.
A Interactions between the ECLs. Black dashed lines indicate hydrogen bonds. **B** Molecular surface of the extracellular side. **C–F** Residues facing pocket A (**C**), pocket B (**D**), pocket C (**E**), and pocket D (**F**).

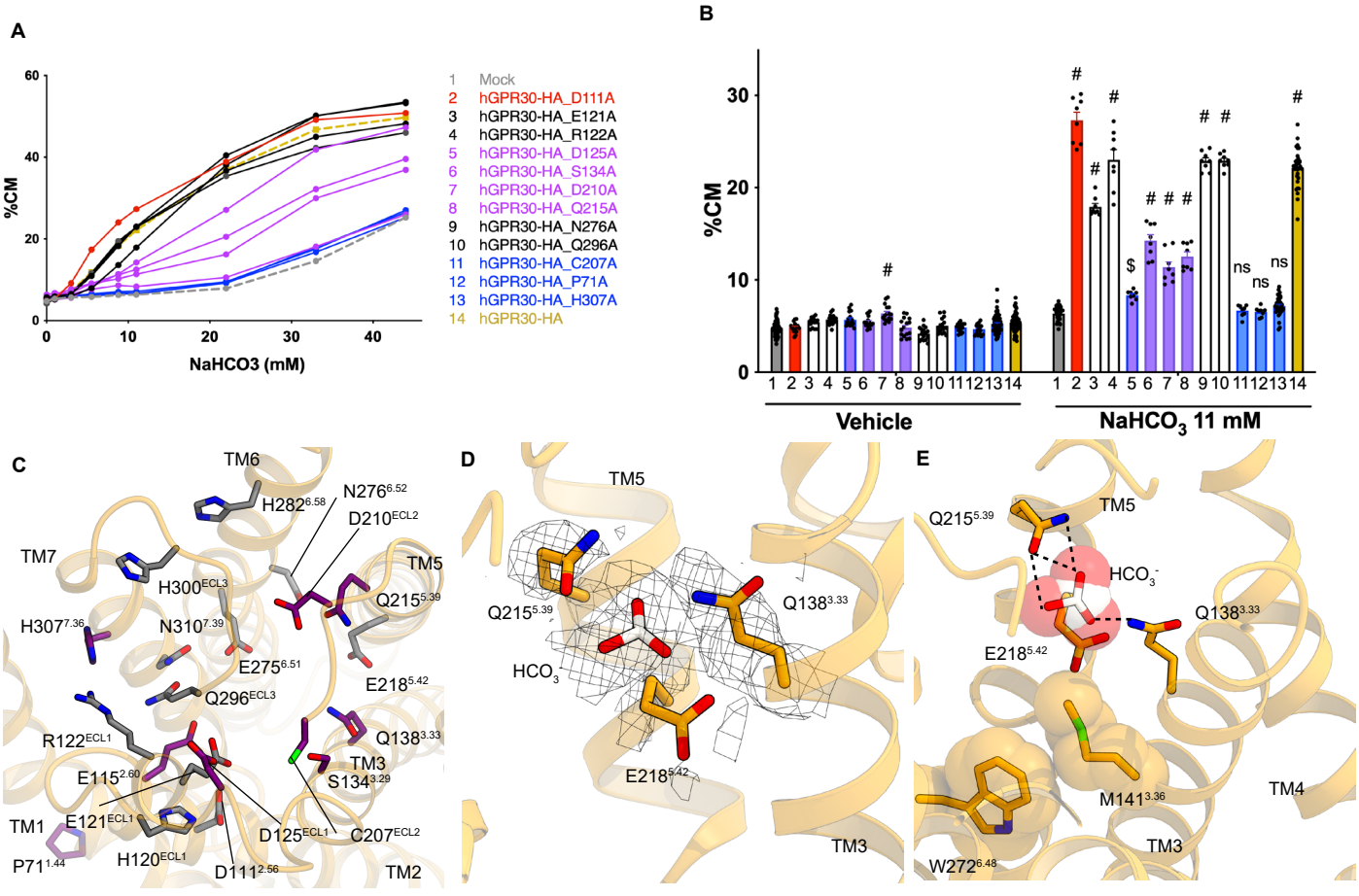

Figure 4. Mutational analysis.

A, B TGFα shedding assay using HEK293 cells transfected with HA-tagged hGPR30. The mutants D111A; C207A, P71A, H307A; and D125A S134A, D210A, Q215A are highlighted in red, blue, and purple, respectively. Statistical analysis:$ p = 0.0001, # p < 0.0001 compared to mock cells using two-tailed unpaired t-test with Bonferroni's correction after two-way ANOVA. ns indicates no significant difference. Data are presented as mean values (c) and mean values ± SEM (d).

C Residues that were subjected to mutant analysis are mapped to the structure. Only residues with reduced bicarbonate responses are colored.in magenta. **D** Density corresponding to bicarbonate. **E** Putative binding mode of bicarbonate. Black dashed lines indicate hydrogen bonds.

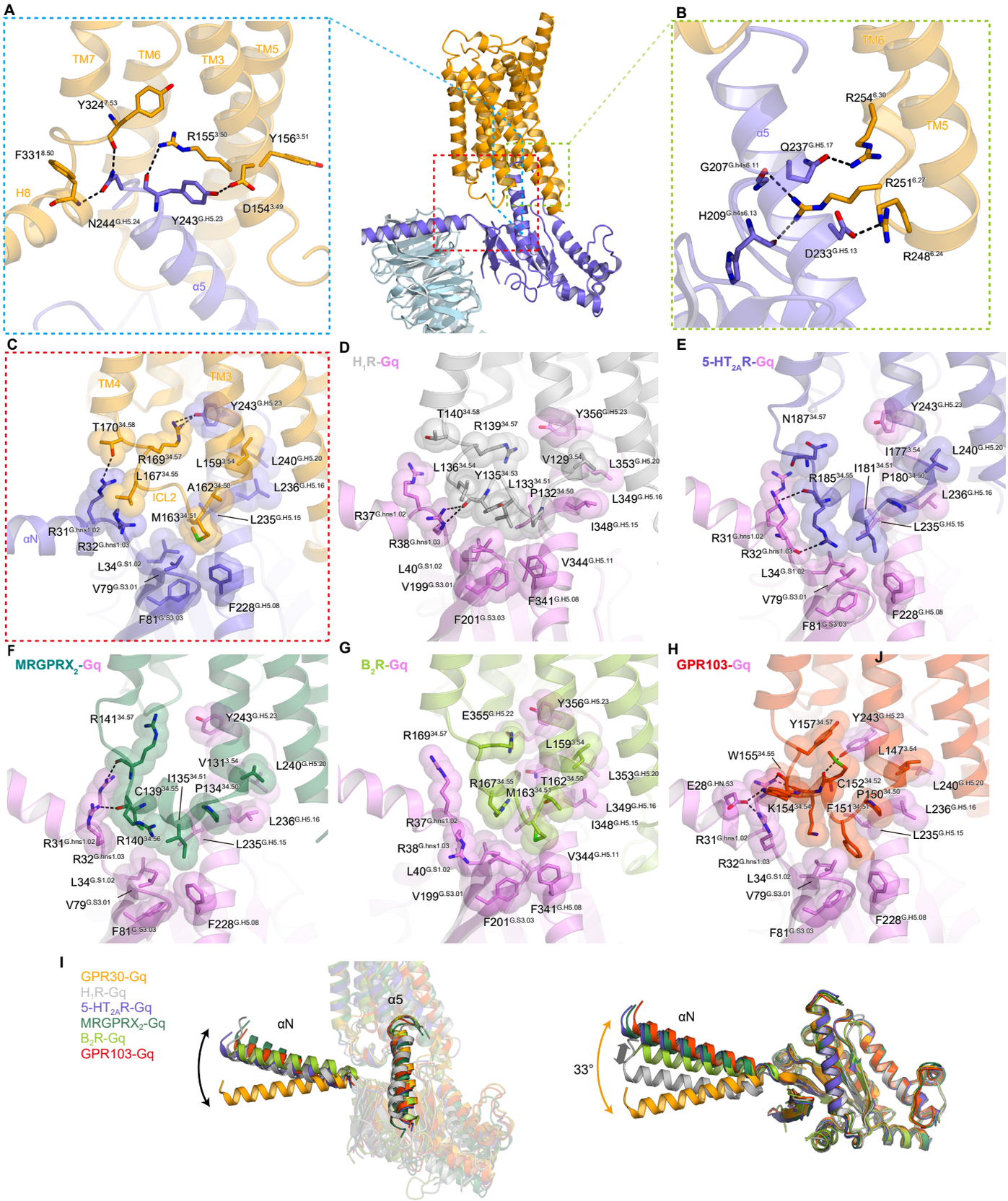

Figure 5. G-protein coupling.

A Hydrogen-bonding interactions between the C-terminal α5-helix residues and the receptor. **B** Electrostatic and hydrogen-binding interactions between ICL3 and the α5-helix. **C–H** Interface between ICL2 and Gq, with residues involved in hydrophobic interactions represented by CPK models. G-protein-bound GPCRs used in the comparison are as follows: H1R-G_q (PDB 7DFL, gray), 5-HT2A-G_q (PDB 6WHA, purple), MRGPRX2-G_q (PDB 7S8L, green), B2R-G_q (PDB 7F6I, yellow-green), and GPR103-Gq (PDB 8ZH8, red). I Comparison of the angles and positions of α5h and αN relative to the receptor. J Superimposition of the Gα subunits.

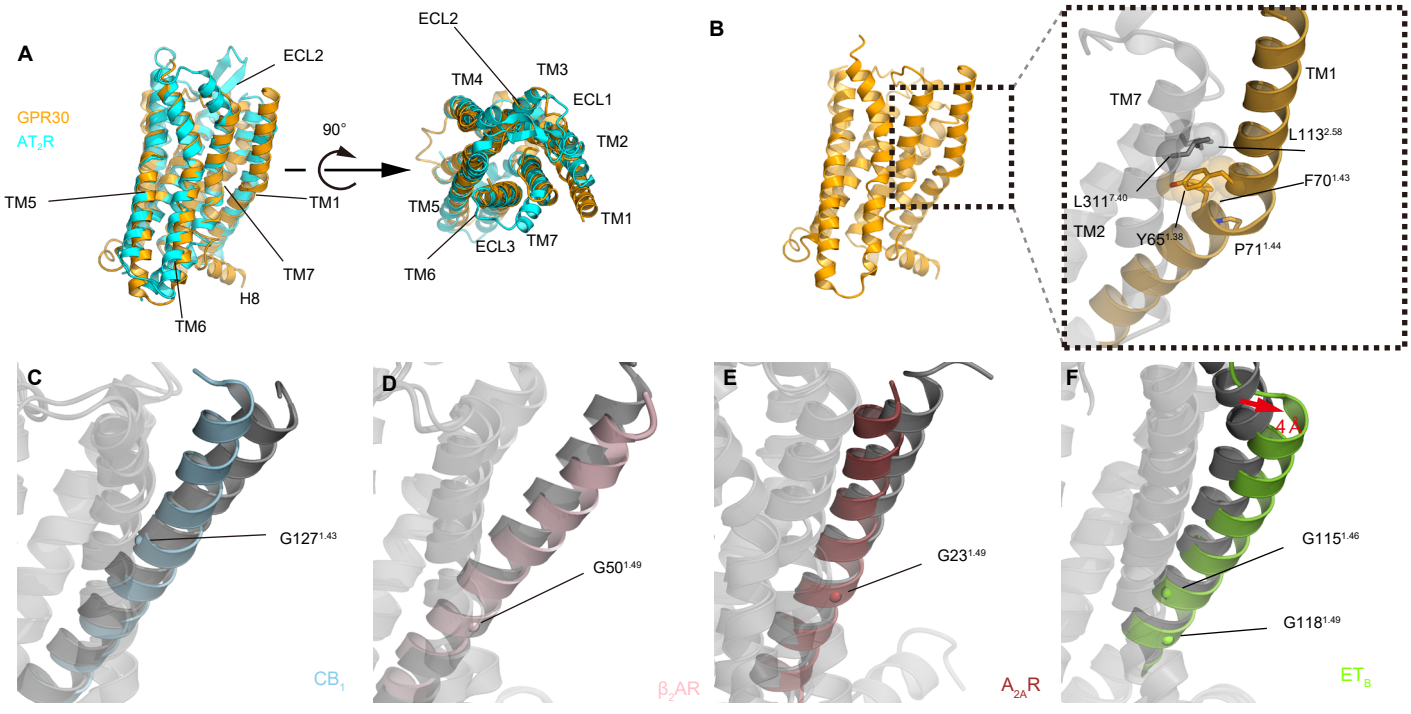

Figure 6. Structural comparison with related GPCRs

A Structural comparison of GPR30 and AT2R (PDB 5UNF). **B** Interactions around P70 in TM1 of GPR30. **C–F** Conformational changes of TM1 upon agonist binding in CB1 (**C**), β2AR (**D**), A2AR (**E**), and ETB (**F**). The agonist-bound states are colored with the respective colors, while the inactive states are colored gray.

The PDB codes used in this figure are CB1-active (PDB 5XRA), CB1-inactive (PDB 5TGZ), β2AR-active (PDB 3SN6), β2AR-inactive (PDB 2RH1), A2AR-active(PDB 6GDG), A2AR-inactive (PDB 3EML), ETB-active (PDB 8IY5), and ETB-inactive (PDB 5X93)..